Applied Surface Science 544 (2021) 148838

Contents lists available at ScienceDirect

Applied Surface Science

journal homepage: www.elsevier.com/locate/apsusc

Full Length Article

Phase-change mechanism and role of each element in Ag-In-Sb-Te: Chemical bond evolution

Dasol Kim [a,b], Taek Sun Jung [a], Hanjin Park [c], Wonjun Yang [a,b], Jeonghwa Han [a,b], Soobin Hwang [a,b], Kyung Ik Sim [a], Young-Kyun Kwon [c], Jae Hoon Kim [a], Mann-Ho Cho [a,b,*]

[a] Department of Physics, Yonsei University, Seoul 03722, Republic of Korea
[b] Atomic-scale Surface Science Research Center, Yonsei University, Seoul 03722, Republic of Korea
[c] Department of Physics and Research Institute for Basic Sciences, Kyung Hee University, Seoul 02447, Republic of Korea

ARTICLE INFO

Keywords:
Phase-change mechanism
Pnictogenide alloy
Role of element
Rapid and energy efficient operation
Storage class memory

ABSTRACT

Reversible phase-change is one of the most promising bases to store data for universal electronic memory. Rapid and energy efficient crystallization of Ag-In-Sb-Te, owing to miniscule atomic displacements, has dragged large interest. However, crystallization mechanism at atomic scale and role of element in Ag-In-Sb-Te remain inconclusive. We studied evolution of chemical bonding on crystallization of Ag-In-Sb-Te, i.e., chemical bonding of element In dramatically changes on crystallization from Sb-bonds (In-Sb) to Te-bonds (In-Te). The local environments of In corresponding to In-Sb and In-Te bonds are characterized as InSb-like and $AgInTe_2$-like site, respectively. Further, In largely modulates the degree of atomic ordering and activation energy for crystallization despite of low composition. The overall results suggest that crystallization of Ag-In-Sb-Te is deployed by the transition of local environment of In from InSb-like to $AgInTe_2$-like site. It suggests role of Ag, In, and Te on crystallization, i.e., Ag provides structural flexibility for transition in local environment of In, In disrupts crystallization, and Te assists the other elements to play their respective roles. The present work on the unique crystallization mechanism of Ag-In-Sb-Te successfully accounts for the memory properties depending on composition and can be applied to development of future memory device.

1. Introduction

Reversible phase-change (crystallization and amorphization) on the subnanosecond scale is one of the most promising bases to store data for nonvolatile universal electronic memory, enabling neuromorphic hardware [1,2]. To develop optimized materials for such memory, role of each element in conventionally utilized materials, namely phase-change materials (PCMs), is required. For example, an umbrella flip model or defective octahedron model [3,4] (Ti-centered octahedron [5,6]), which clarified the role of each element in pseudobinary compound GeTe-Sb_2Te_3 ($Ti_{0.32}Sb_2Te_3$), successfully inspired ones to develop GeTe-Sb_2Te_3 superlattice structure [7] ($Sc_{0.2}Sb_2Te_3$ [8,9]) as an enhanced PCM. However, the role of each element in Ag-In-Sb-Te is still under debate although its memory properties are outstanding, especially rapid and energy efficient operation [10–12].

Various compositions of Ag-In-Sb-Te have been developed and utilized for optical storage technologies since Iwasaki *et al.* first reported on $Ag_{11}In_{11}Sb_{55}Te_{23}$ (denoted by the yellow circle in Fig. 1 a [13–16]) in 1992. Remarkable researches on Ag-In-Sb-Te have been reported in the respect to fragility, diffusivity, growth velocity, and local structures [17–24]. Among them, role of each element in Ag-In-Sb-Te has been also proposed, i.e., in the case of Sb, experimental result that local structures of Sb in both amorphous and crystalline $Ag_{3.5}In_{3.8}Sb_{75.0}Te_{17.7}$ (denoted by the blue circle in Fig. 1 a) are distorted octahedrons with three short and three long bonds [10] suggests that crystallization occurs in the form of consecutive atomic arrangements driven by the interchange between short and long bonds of Sb, namely a bond-interchange model. The bond-interchange model successfully clarifies the role of Sb and compares it to an *avalanche*.

On the other hand, Hiroko *et al.* and Zhu *et al.* successfully suggested roles of Ag and In in $Ag_5In_5Sb_{60}Te_{30}$ (denoted by the red circle in Fig. 1 a [23,25–28]); i.e., both Ag and In stabilize the amorphous phase, while In additionally promotes the crystallization speed [11,29]. However, these models can neither fully explain the mechanism leading to the bond-interchange of Sb (crystallization) at atomic scale nor can they illustrate the several experimental results such as great dependence of

* Corresponding author at: Department of Physics, Yonsei University, Seoul 03722, Republic of Korea.
E-mail address: mh.cho@yonsei.ac.kr (M.-H. Cho).

https://doi.org/10.1016/j.apsusc.2020.148838
Received 11 September 2020; Received in revised form 23 November 2020; Accepted 22 December 2020
Available online 25 December 2020
0169-4332/

thermal stability on compositions in Ag-In-Sb-Te. The unsolved territory in role of each element in Ag-In-Sb-Te can be resolved by clarifying crystallization mechanism at atomic scale. Unlike crystallization of glasses such as SiO_2 [30,31], crystallization of PCMs are deployed by transition of local environment from a second stable local environment (2nd-SLE) to a first stable local environment (1st-SLE) as shown in Fig. 1 b. For example, crystallization of Ge-Sb-Te is deployed by transition of local environment of Ge from tetrahedral (or defective octahedral) to octahedral sites [3,4]. Unfortunately, 1st-SLE and 2nd-SLE in Ag-In-Sb-Te are yet to be clarified because the direct analysis of local structural characteristics, such as bond length or coordination number, of Ag and In in amorphous Ag-In-Sb-Te is practically impossible. The complexity induced by four elements in similar atomic numbers and compositional scarcity of Ag and In in Ag-In-Sb-Te make it hard to analyse them with X-ray absorption spectroscopy (XAS) and Raman spectroscopy.

In our study, we studied the evolution of chemical bond of each element on crystallization of Ag-In-Sb-Te rather than direct analysis on local structural characteristics. It is shown by *in-situ* X-ray photoelectron spectroscopy (XPS) that element In dramatically changes its chemical bonding on crystallization from Sb-bonds (In-Sb) to Te-bonds (In-Te), where corresponded local environments are characterized as that of InSb and $AgInTe_2$, respectively by density functional theory calculation (DFT calculation). Further, we proceed experimental verifications for the structural characteristics of the suggested local environments with optical/electrical macroscopic properties, i.e., In critically modulates the degree of atomic ordering and activation energy for crystallization despite of low composition (4%). The overall results suggest crystallization is deployed by the transition of local environment of In from InSb-like to $AgInTe_2$-like site. The 'dam-gate model' is proposed for role of element Ag, In, and Te and accounts for the unsolved phase-change properties depending on composition. Unique phase-change mechanism of Ag-In-Sb-Te is described at atomic scale and compared with that of the most popular PCM, Ge-Sb-Te.

2. Experimental section

2.1. Sample preparation

The ST, IST, AST, AIST, and $AIST_{Eutectic}$ films were fabricated by Ar^{+} ion beam sputtering using each single target with the desired composition in an ultrahigh vacuum (UHV) chamber. The base pressure and working pressure of the UHV chamber were 3.0×10^{-8} Torr and 6.5×10^{-5} Torr, respectively. Compositions were confirmed with *in-situ* XPS. The amorphous (crystal) structure of the as-deposited (annealed) films was confirmed with X-ray diffraction and Raman spectroscopic measurements. Fifty-nanometer thick PCMs for XPS were deposited on highly doped Si to exclude the charging effect; 100–1000 nm-thick PCMs were deposited on the Si and annealed above the crystallization temperature for IR-SE.

2.2. in-situ XPS

In-situ XPS analyses of the core levels were conducted using a PHI 5000 VersaProbe instrument (ULVAC-PHI), where the base pressure was 5.0^{-10} Torr. XPS results were recorded using monochromatic Kα radiation with analyzer pass energies of 23.5 eV and 11.75 eV. The background of each spectrum was subtracted by the Shirley method.

2.3. Density functional theory calculation

To explore the structural properties and the transition behavior between the crystal and amorphous phases of AIST, we used *ab initio* DFT calculations [32] based on a linear combination of atomic orbitals, as implemented in the SIESTA code [33,34], and reproduced the $Ag_1In_1Sb_{18}Te_4$ cell for the crystal phase and that of $Ag_8In_8Sb_{144}Te_{32}$ for the amorphous phase. Double-ζ polarization was used as a basis set to expand the electronic wave functions. The behavior of the valence electrons was described by the norm-conserving Troullier-Martins pseudopotential [35] with partial core corrections in the Kleinman-Bylander factorized form [36]. We considered the $4d^{10}5s^1$, $5s^25p^1$, $5s^25p^3$, and $5s^25p^4$ electrons as the valence level in the pseudopotentials for Ag, In, Sb, and Te, respectively. We used the Perdew-Zunger form [37] of the Ceperley-Alder exchange–correlation (XC) functional [38] within the local density approximation. The charge density and potentials were determined on a real-space grid with a mesh cutoff energy of 210 Ry. We used a confinement energy shift of 0.02 eV, which defines the cutoff radii of atomic orbitals.

To identify the local atomic characteristics, we carried out molecular

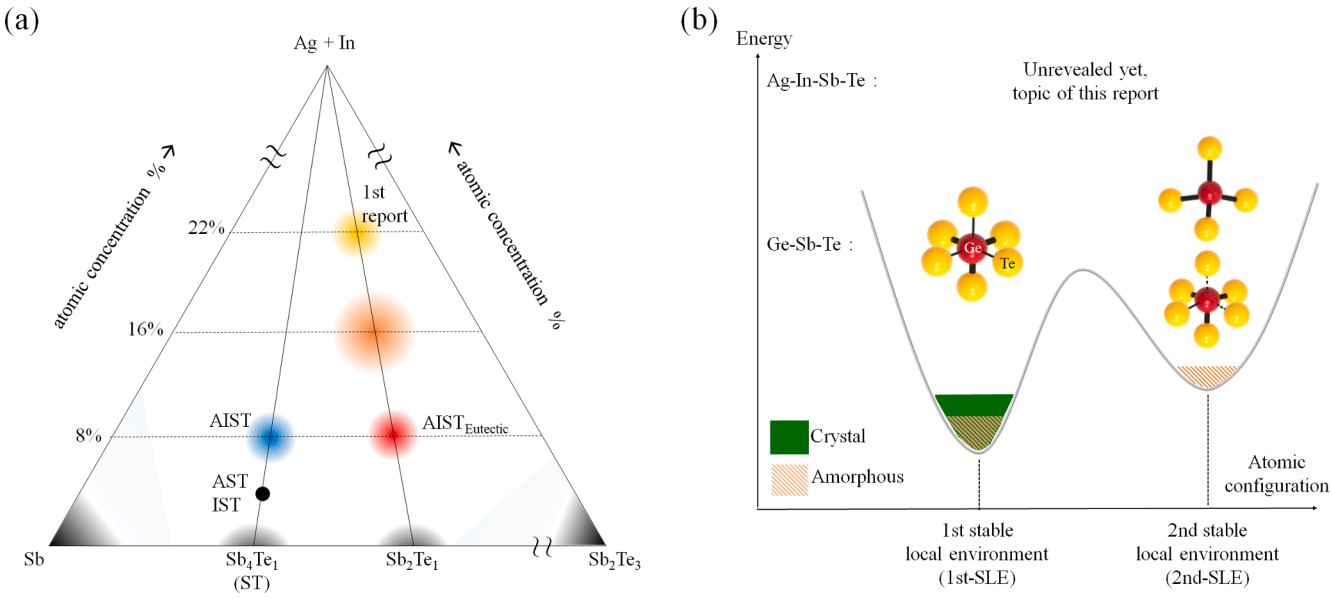

Fig. 1. Phase-diagram of Ag-In-Sb-Te and local environments of phase-change materials. (a) Phase-diagram of Ag-In-Sb-Te. Previously reported compositions appear in color. (b) Local environments of PCMs can be classified into energetically 1st and 2nd stable local environments. The local environment of crystalline PCMs consists of a 1st stable local environment, whereas those of amorphous PCMs consist of both 1st and 2nd stable local environments. The crystallization and amorphization of PCMs are deployed by the local environment transitions of certain element that differ considerably from the continuous random network model.

dynamics (MD) simulations within the canonical ensemble while changing various conditions such as the temperature, density, and initial configurations. We solved the classical equation of motion with the quantum mechanical force acting on each atom, which was calculated by applying the Hellmann-Feynman theorem. The target temperature was controlled by adjusting the temperature of the heat bath using a Nosé thermostat [39–42]. In our calculations, we considered a unit cell containing 24 (192) atoms for the crystal (amorphous) phases. To identify the most stable crystal phase, we considered various configurations with different site locations of the Ag, In, Sb, and Te atoms. To find the equilibrium structure of each configuration, we maintained the $R3\_m$ symmetry with lattice parameters of $a = b = 8.77$ Å but adjusted the parameter c until the energy was minimized [27]. The calculated c values were in the range 10.12–10.36 Å. To produce the amorphous phase, we performed MD-based melt-quench simulations, mimicking a real amorphization process. To reduce the computational cost, we first executed MD simulations at a high temperature (approximately 5000 K) and with a low density (approximately 45% lower than its ambient value of 0.030 atom/Å^3 at 300 K by expanding the unit cell). This process is known as pre-melting and is performed to completely scatter atoms. Then, we continued our MD simulations by lowering the temperature to approximately 1000 K with its ambient density imitating the liquid phase. After the system attained equilibrium at T = 1000 K, we employed a quenching process while decreasing the temperature at a rate of 10.8 K/ps until room temperature (300 K) was attained. During every MD simulation, we collected the coordinates $\{\mathbf{r}_i\}$ and velocities $\{\mathbf{v}_i\}$ ($i = 1, 2, 3, \cdots, N$) of all atoms with which we analyzed their various structural properties. Angle distribution functions of atoms are considered within the cutoff radius of 0.35 nm.

2.4. Infrared spectroscopic ellipsometry

Ellipsometry spectra were measured in the range of 0.08–0.7 eV using a Sopra GES5 instrument with an angle of incidence of 60° at 300 K. A globar source and a mercury cadmium telluride (MCT) detector were used for mid-FTIR spectroscopy with a resolution of 2 meV. The models of dielectric functions for fitting were based on the Drude and Tauc-Lorentz models. The Drude model describes the intraband excitation and assumes the motion to resemble that of a classical gas of electrons, whereas the Tauc-Lorentz model exhibits an interband transition above the band edge. ϵ_∞, which is the background permittivity from higher frequency oscillators, is included in the Tauc-Lorentz model. The low-energy dielectric constant was set at 0.08 eV. The dielectric functions for ST, IST, AST, AIST, and AIST$_{\text{Eutectic}}$ with at least three thicknesses (100 nm–1 μm) were examined for reliability.

2.5. Hysteresis of electrical resistance on temperature (R-T)

The measurements are executed after few times of alternating vacuum pumping and N_2 purging. Constant current mode at 5 mA for two points probe is utilized. Sample width and length are 1 mm and 2 mm, respectively. Thicknesses of samples exceed 300 nm, which is enough to represent bulk properties.

3. Results and discussion

3.1. Chemical bond characterization by in-situ XPS

We study evolution of chemical bonding for each constituent element on crystallization of AIST via *in-situ* XPS, element selective tool [3,43]. Among them, element In represents the largest change while the other elements in AIST (Ag, Sb, and Te) represent negligible change as detailed in Supplementary Fig. S1. As is apparent from Fig. 2 a, the shape of the spectrum of In $3d_{5/2}$ core level in crystalline AIST (denoted by the blue circle in Fig. 1 a) is symmetric with a binding energy of 444.7 eV, which is in the range of Te bonds (In-Te), i.e., In mainly bonds with Te (In-Te) in crystalline AIST [44–46]. However, the spectrum of In $3d_{5/2}$ core level in amorphous AIST is asymmetric, which indicates the coexistence of different type of chemical bonding [43]. We confirmed that the spectrum of In in amorphous AIST subtracted from that in crystalline

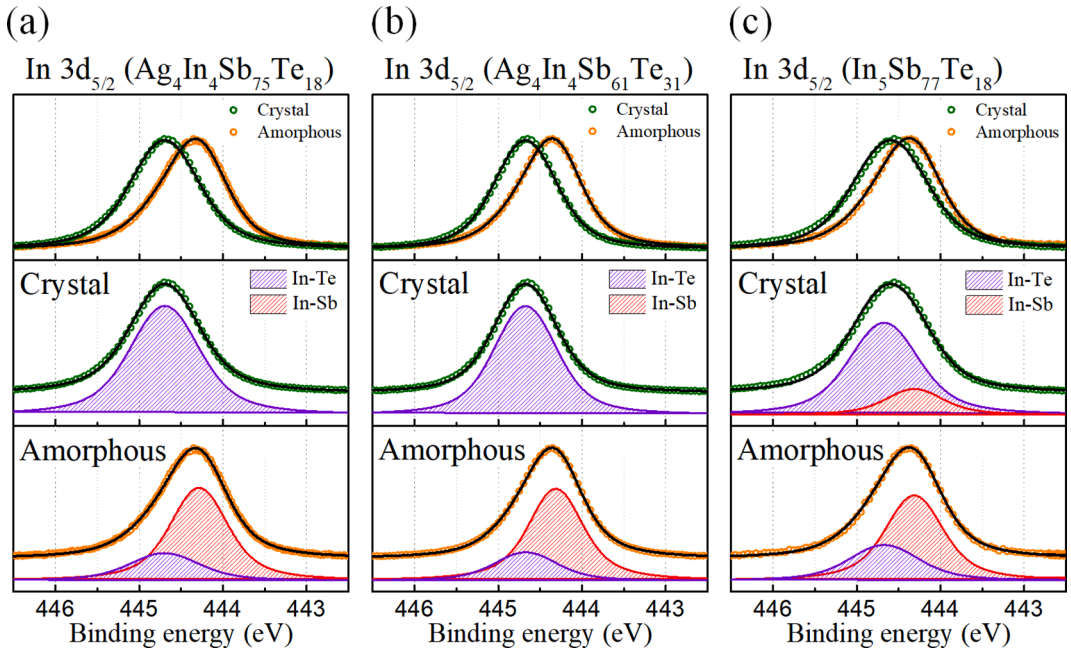

Fig. 2. Local environments of In in amorphous and crystalline $Ag_4In_4Sb_{75}Te_{18}$ (AIST), $Ag_4In_4Sb_{61}Te_{31}$ (AIST$_{\text{Eutectic}}$), and $In_5Sb_{77}Te_{18}$ (IST). The three columns represent the deep core level spectra of In $3d_{5/2}$ in (a) AIST, (b) AIST$_{\text{Eutectic}}$, and (c) IST, respectively, obtained using X-ray photoelectron spectroscopy. Measured data and fitted lines are shown in the form of a set of circles and black lines, respectively, with the crystalline (amorphous) data are plotted in green (orange). The upper panels show the crystalline and amorphous measured data and fitted lines simultaneously for comparison. The middle (lower) panels show the measured data and fitted lines for the deconvoluted spectra of crystalline (amorphous) sample. Spectra of In-Te bonds are in purple and those of In-Sb bonds in red. (For interpretation of the references to color in this figure legend, the reader is referred to the web version of this article.)

AIST with reduced intensity is also symmetric and has the same Gaussian-Lorentzian width. Thereby, asymmetry of the 3d spectrum of In is resolved into two symmetric peaks, where the second peak of In in amorphous AIST with a binding energy of 444.3 eV is in the range of Sb bonds (In-Sb) [45,47]. There are two types of In in amorphous AIST, where bonding of each type is dominated by Sb (In-Sb) or Te (In-Te). The result that crystallization of AIST is deployed by large chemical bond evolution of In from In-Sb to In-Te suggests that local environments of In whose bonding is dominated by Te and Sb be a 1st-SLE and 2nd-SLE of AIST, respectively. In the case of $AIST_{Eutectic}$ (denoted by the red circle in Fig. 1 a), spectra of element in amorphous and crystalline $AIST_{Eutectic}$ exhibits same feature with those of AIST (denoted by the blue circle in Fig. 1 a), respectively as shown in Fig. 2 and Supplementary Fig. 1. It indicates that chemical bond evolution on crystallization of $AIST_{Eutectic}$ is identical to that of AIST.

In the case of amorphous IST, the spectrum of In $3d_{5/2}$core level represents negligible difference with those of amorphous AIST and $AIST_{Eutectic}$. However, spectrum of In in crystalline IST shows clearly distinguishable features in comparison with those in crystalline AIST and $AIST_{Eutectic}$, i.e., the spectrum is asymmetric as specifically depicted in Fig. 2 c. In particular, the spectrum of In in crystalline IST is even broader, compared to that in amorphous IST, which is highly atypical because the chemical bonding in crystalline phase is typically more confined than that in amorphous phase. The unusual broadness of the spectrum of In in crystalline IST results from the coexistence of two types of chemical bond of In, In-Te and In-Sb as shown in Fig. 2 c. Even after crystallization, residual In-Sb co-exists with In-Te in IST. It is remarkable that the absence of Ag critically discourages the chemical bond evolution of In from In-Sb to In-Te despite of low composition of Ag (4%) and In (4%).

Chemical bonding of Ag in amorphous and crystalline AIST, $AIST_{Eutectic}$, and AST films is identified in Fig. 3. The spectra of Ag $3d_{5/2}$ of amorphous and crystalline AIST, $AIST_{Eutectic}$, and AST are symmetric and identical. The spectrum of the Ag $3d_{5/2}$ core level, with a binding energy of 368.3 eV in the range of Te bonds [48] shows that Ag always bonds with Te (Ag-Te) in AIST, $AIST_{Eutectic}$, and AST, regardless of phase. The result that chemical bonding of Ag does not undergo any variation during the crystallization of AIST, $AIST_{Eutectic}$, and AST, indicates that Ag does not directly participate in the crystallization process.

3.2. Local environment characterization by DFT calculation

To verify and further characterize the chemical bonding of Ag and In in crystalline AIST, we computationally reproduced the crystal structure of AIST and calculated the total energy of the structure varying its atomic configurations by first-principle DFT calculations, as depicted in Fig. 4 a. Even though the atomic sites in the crystal structure of AIST are reportedly randomly occupied by composite elements, an energy hierarchy in terms of the exchange of elements still exists in the structures we reproduced. Specifically, we reproduced 12 types of atomic configurations of the crystalline $Ag_1In_1Sb_{18}Te_4$ structure and eventually categorized them into five groups according to the number of Te atoms that simultaneously bond with Ag and In (Ag-Te-In). They showed clear energy hierarchy according to the number of Ag-Te-In unit, i.e., the cell becomes the most stable when the number of Ag-Te-In units is maximized to four. Further, the cells were monotonically destabilized as the number of Ag-Te-In unit decrease. Ag-Te-In unit stabilizes the total energy of structure. The result is consistent with the experimental results obtained by XPS that Ag and In mainly bonds with Te (Ag-Te and In-Te) in crystalline AIST. Further, energy destabilization on deviation of Ag-Te-In unit in the reproduced crystalline structure accounts for the result obtained by XPS that absence of Ag discourages the chemical bond evolution of In from In-Sb to In-Te. The result is also consistent with existing experimental reports according to which single-phase crystalline $Ag_{3.4}In_{3.7}Sb_{76.4}Te_{16.5}$ (denoted by the blue circle in Fig. 1 a) becomes phase-separated into $AgInTe_2$, Sb, and Sb_2Te_3 crystals when annealed above the crystallization temperature [49,50]. As bonding topology of Ag-Te-In is identical to that of the $AgInTe_2$ crystal, "$AgInTe_2$-like site" is suggested as a local environment of In whose bonding is dominated by Te (In-Te) i.e., $AgInTe_2$-like site of In is the 1st-SLE of

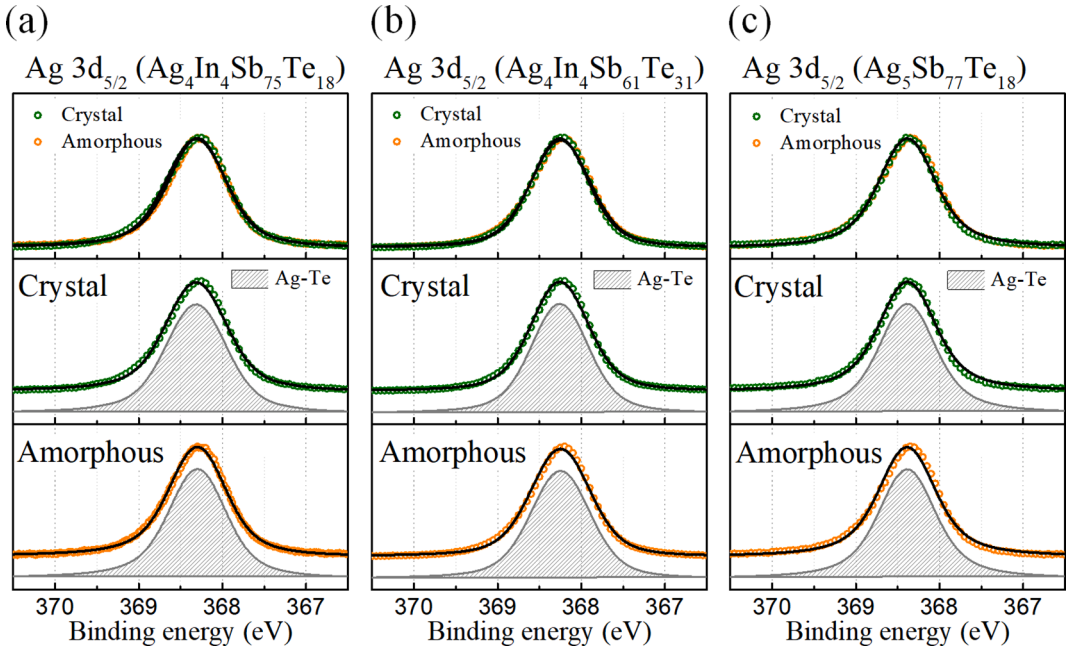

Fig. 3. Local environments of Ag in amorphous and crystalline $Ag_4In_4Sb_{75}Te_{18}$ (AIST), $Ag_4In_4Sb_{61}Te_{31}$ ($AIST_{Eutectic}$), and $Ag_5Sb_{77}Te_{18}$ (AST). The three columns represent the deep core level spectra of Ag $3d_{5/2}$ in (a) AIST, (b) $AIST_{Eutectic}$, and (c) AST, respectively, obtained with X-ray photoelectron spectroscopy. The measured data and fitted lines are shown in the form of a set of circles and black lines, respectively, where the crystalline (amorphous) data are plotted in green (orange). The upper panels show the crystalline and amorphous measured data and fitted lines simultaneously for comparison. The middle (lower) panel shows the measured data and fitted lines for the deconvoluted spectra of crystalline (amorphous) sample. Spectra of Ag-Te bonds are in gray. (For interpretation of the references to color in this figure legend, the reader is referred to the web version of this article.)

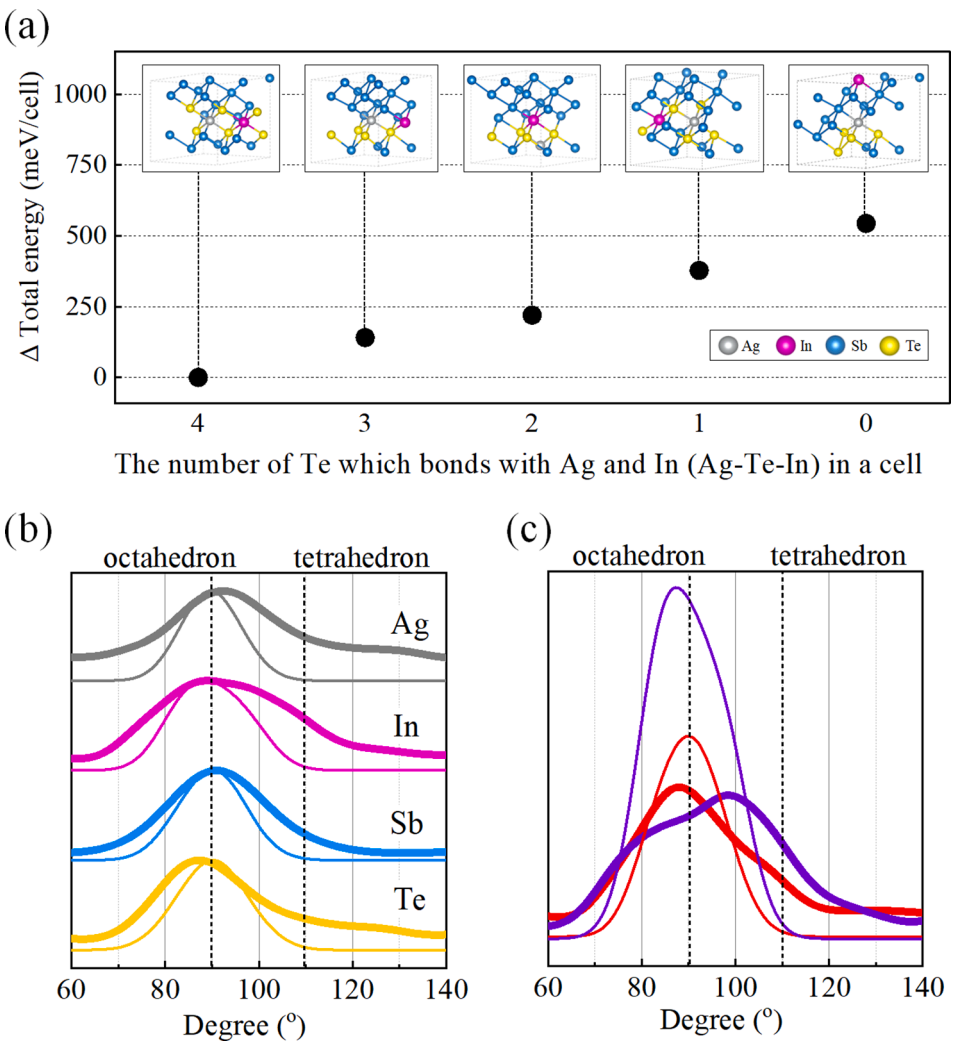

Fig. 4. Total energy of various crystalline $Ag_1In_1Sb_{18}Te_4$ cells and structural analysis of crystalline and amorphous cells. (a) Crystalline $Ag_1In_1Sb_{18}Te_4$ cells with 12 different atomic configurations classified into five groups according to their local environment and energy hierarchy with Ag, In, Sb, and Te atoms shown in gray, magenta, blue, and yellow, respectively, with the total energy. (b) Angle distribution function (ADF) of amorphous and crystal structure plotted with thick and thin lines, respectively, with the angle distributions of Ag, In, Sb, and Te plotted in gray, magenta, blue, and yellow, respectively. (c) Specific ADF of the element In in amorphous and crystalline structures plotted in thick and thin lines, respectively, with the angle distributions of Sb-In-X plotted in red and those of Te-In-X in purple, respectively. (For interpretation of the references to color in this figure legend, the reader is referred to the web version of this article.)

AIST.

For further study of chemical bonding of elements in amorphous and crystalline AIST, we computationally reproduced additional amorphous $Ag_8In_8Sb_{144}Te_{32}$ supercells and performed molecular dynamics (MD) simulations for both amorphous and crystalline cells for a period of 5 ps at 300 K within canonical ensembles. We analyzed the structural characteristics of these supercells by using the angle distribution function (ADF) and radial distribution function (RDF) to compute the respective elemental distributions, as shown in Fig. 4 b, c, and Supplementary Fig. S3, respectively. As depicted in Fig. 4 b, the angle distribution of each element in the amorphous and crystal structure of AIST is centered at 90°, which is consistent with existing reports that the local environment in amorphous and crystalline AIST is mainly octahedral [10,51].

We further analysed the angle distributions of In in both amorphous and crystal structures by classifying them into patterns corresponding to the Sb-In-X and Te-In-X angles, where X represents any element in AIST, as depicted in Fig. 4 c. The population ratio of the pattern corresponding to the angle of Te-In-X over that of Sb-In-X is considerably larger in the crystal structure than that in amorphous AIST structure. This result is consistent with the experimental result obtained by XPS—In-Te dominates in crystalline AIST while In-Te and In-Sb coexist in amorphous AIST. The distributions corresponding to both Sb-In-X and Te-In-X angles in the amorphous structure are clearly asymmetric. They can be deconvoluted into a distribution centered at 90° and an additional distribution centered between 100° and 110°, i.e., the local environments of In in amorphous AIST consist of both octahedron and tetrahedron. This is clearly distinguished with those of Ag, Sb, and Te in amorphous AIST, which mainly consist of octahedron as depicted in Supplementary Fig. S4. The additional tetrahedral local environment of element In corresponds to In-Sb bonding, which is an additional bonding type of element In in amorphous AIST in comparison with that in crystalline AIST. It is consistent with the reports that local environment of In is dominated by 4-fold tetrahedron unlike Ag, Sb, and Te in melt-quenched $Ag_{20}In_{16}Sb_{360}Te_{144}$cell reproduced by MD simulations [17]. As tetrahedral local environment of element In which bonds with Sb is identical to bonding topology of the InSb crystal, "InSb-like site" is suggested as a local environment of In whose bonding is dominated by Sb in AIST, i.e., InSb-like site of In is the 2nd-SLE of AIST. Tetrahedral local environment of InSb-like site of element In in AIST is expected to deviate octahedral local environment in Ag-In-Sb-Te and degrade the degree of atomic ordering. At the point, we proceed experimental verification for the structural characteristics of the suggested local environments, evaluating atomic middle range order (AMRO) with varying compositions.

3.3. Optical properties and AMRO characterization obtained by IR-SE

The nature of bonding in crystalline PCMs is in stark contrast to that in amorphous PCMs; i.e., the valence electrons in crystalline PCMs are spatially more delocalized compared to those in amorphous PCMs, similar to resonant bonding [52,53]. A new type of bonding, termed metavalent bonding, exclusively appears when PCMs have the atomic middle or long range order. Conversely, the degree of atomic middle

range order (AMRO) can be characterized based on the degree of electron delocalization or metavalent bonding, which is quantified using the dielectric constant under a static electric field without free carrier contributions. Supplementary Fig. S5 shows the dielectric functions of both amorphous and crystalline ST, IST, AST, AIST, and $AIST_{Eutectic}$ in the infrared (IR) region. They include a single Tauc-Lorentz oscillator term, whereas only those of crystalline PCMs involve an additional single Drude term to account for free carriers, which is consistent with the reports [52,53]. Fig. 5 a depicts ϵ_1 without the Drude contribution in the IR region, where the values of ϵ_∞, the DC limit of a real value of the dielectric function ϵ_1, for the amorphous films (21–28) are relatively low, compared to those of the crystalline films (37–67), indicating that the bonding types of the amorphous and crystalline films are covalent and metavalent, respectively. The formation of the AMRO after crystallization is quantified by the formula, $\epsilon_\infty^{cry}/\epsilon_\infty^{amorphous}-1$, as presented in Fig. 5 b. The value of $\epsilon_\infty^{cry}/\epsilon_\infty^{amorphous}-1$ exceeding 100% in ST, AST, AIST, and $AIST_{Eutectic}$, which is comparable to those of other PCMs [52,53], indicates that crystallization, which accompanies improvement on AMRO, successfully leads compounds to form metavalent bonding.

Remarkably, the value of ϵ_∞ for crystalline IST (46) is relatively lower than those for crystalline ST, AST, AIST, and $AIST_{Eutectic}$, indicating the deficient AMRO of crystalline IST. The result obtained by XPS and DFT calculations that residual In in InSb-like site exists in crystalline IST in the form of tetrahedron successfully accounts for critical degradation of atomic ordering in octahedron. Further, deficient AMRO in crystalline IST is recovered by doping with Ag, comparing % increase of ϵ_∞ of IST (70%) with AIST (132%) as shown in Fig. 5 b, i.e., In in $AgInTe_2$-like site is relatively cooperative to form the AMRO rather than that in InSb-like site. Structural characteristics of the local environments of In, obtained by combining the results of XPS and DFT calculations, are successfully verified through macroscopic optical properties, i.e., In largely modulates the degree of atomic ordering and that in the InSb-like site critically degrades AMRO.

3.4. Crystallization kinetics obtained by hysteresis of electrical resistance on temperature

We further proceed experimental verification for effects of dopants (Te, Ag, and In) on thermal stability of amorphous phase. Hysteresis of electrical resistance on temperature (R-T) during annealing and cooling is shown in Fig. 6a, starting from amorphous phase. The thermal hysteresis can be classified into three regimes as indicated by black arrows. On annealing process, first regime shows gradual decrease in electrical resistance, while second regime shows sudden drop of electrical resistance in the range between 90 °C and 150 °C, owing to crystallization which is confirmed by structural analysis based on the results of Raman spectroscopy and X-ray diffraction (XRD). Third regime shows negligible change in electrical resistance on cooling, indicating no structural change in crystalline film. Crystallization temperature is defined as the point where electrical resistance suddenly drops that derivative of log R is minimized. Crystallization temperatures of ST, AST, and AIST films are 104.6, 125.7, and 140.1 °C, respectively. Doping element in the order of Te, Ag, and In into Sb monotonically increases crystallization temperature, where pure Sb spontaneously crystallizes at room temperature as shown in Fig. 6b [54]. For further analysis, activation energies for crystallization from amorphous phase are studied via combining Arrhenius and Kissinger models that phase-change speed is maximized at the crystallization temperature and proportional to exp ($-E_a/k_BT$), where E_a, k_B, and T stands for activation energy, Boltzmann constant ($1.380*10^{-23}$ J/K), and temperature, respectively [55]. With the models, activation energies are derived based on the results of crystallization temperature depending on various ramping rates as shown in Fig. 6b and Supplementary Fig. S7 and S8 [13]. Activation energy for crystallization also monotonically increases as the number of dopants increases in the same manner of crystallization temperature. Incorporating 20 at. % Te into pure Sb critically increases activation energy up to 1.67 eV from negligible value [54]. Incorporating additional 5 at. % Ag into ST slightly increases activation energy up to 1.96 eV. However, incorporating additional 4 at. % In into AST largely increases activation energy up to 3.12 eV. The result obtained by R-T that In critically stabilizes amorphous phase is consistent with the results obtained by XPS, DFT calculations, and IR-SE that In critically disturbs crystallization (atomic alignment) in comparison with Ag.

3.5. Memory properties described based on the phase-change mechanism and role of each element in Ag-In-Sb-Te

The results of XPS, DFT calculations, IR-SE, and R-T suggest $AgInTe_2$-like and InSb-like site as the 1st-SLE and 2nd-SLE of AIST, respectively. They are pictured at the bottom of Fig. 7 where three-dimensional atomic configurations of AIST were simplified into two-dimensional schemes. Element In in the 2nd-SLE, InSb-like site, inclines toward Sb rather than Te and deviates local environments of surrounding Sb from the well aligned octahedron to tetrahedron. On the other hand, element In in the 1st-SLE, $AgInTe_2$-like site, forms bond with Te (In-Te) and releases Sb from InSb-like site. Our results propose the crystallization

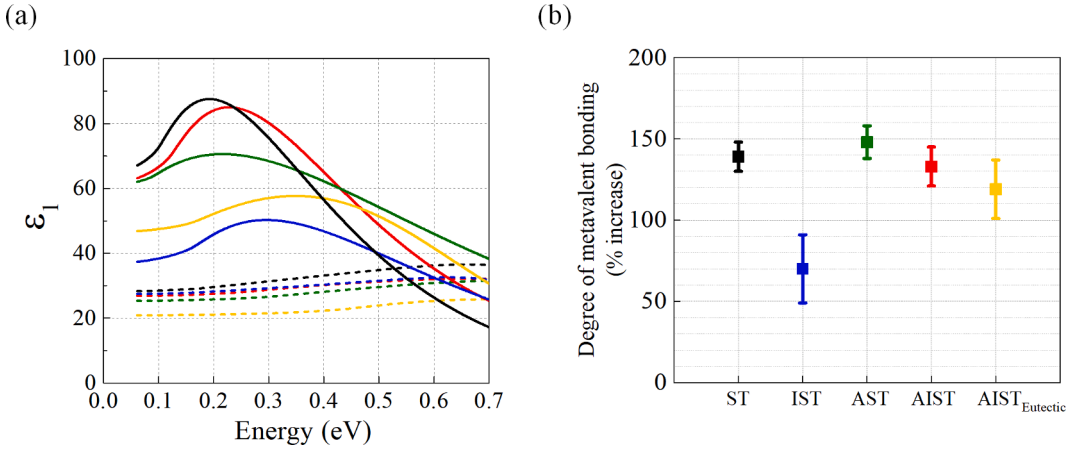

Fig. 5. Dielectric functions of amorphous and crystal PCMs in the infrared range. (a) Real part of dielectric functions of amorphous and crystalline $Sb_{80}Te_{20}$ (ST), $In_5Sb_{77}Te_{18}$ (IST), $Ag_5Sb_{77}Te_{18}$ (AST), $Ag_4In_4Sb_{75}Te_{18}$ (AIST), and $Ag_4In_4Sb_{61}Te_{31}$ ($AIST_{Eutectic}$) without the Drude contribution are plotted in black, blue, green, red, and yellow, respectively, with crystalline and amorphous films represented by solid and dashed lines, respectively. (b) Degree of metavalent bonding quantified with $\epsilon^{\infty}{}_{cry}/\epsilon^{\infty}{}_{amorphous}-1$, where ϵ^{∞} represents the DC limit of the real value of the dielectric function ϵ_1. (For interpretation of the references to color in this figure legend, the reader is referred to the web version of this article.)

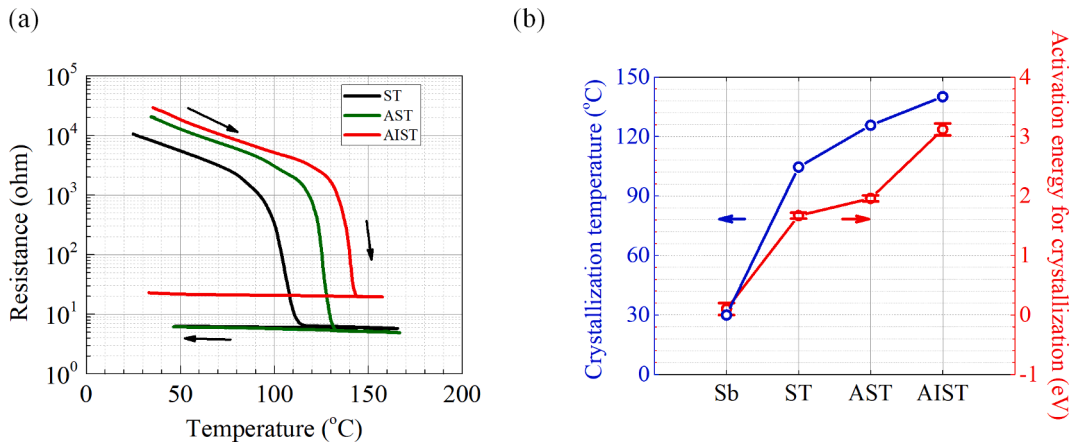

Fig. 6. Resistance dependence on temperature during annealing and cooling process of ST, AST, and AIST. (a) Electrical resistance dependence on temperature on annealing and cooling with 1 °C/min ramping rate, where arrow represents chronological order. Data corresponding to ST, AST, and AIST is colored black, green, and red, respectively. (b) Activation energies for crystallization and crystallization temperatures on composition of thin films. (For interpretation of the references to color in this figure legend, the reader is referred to the web version of this article.)

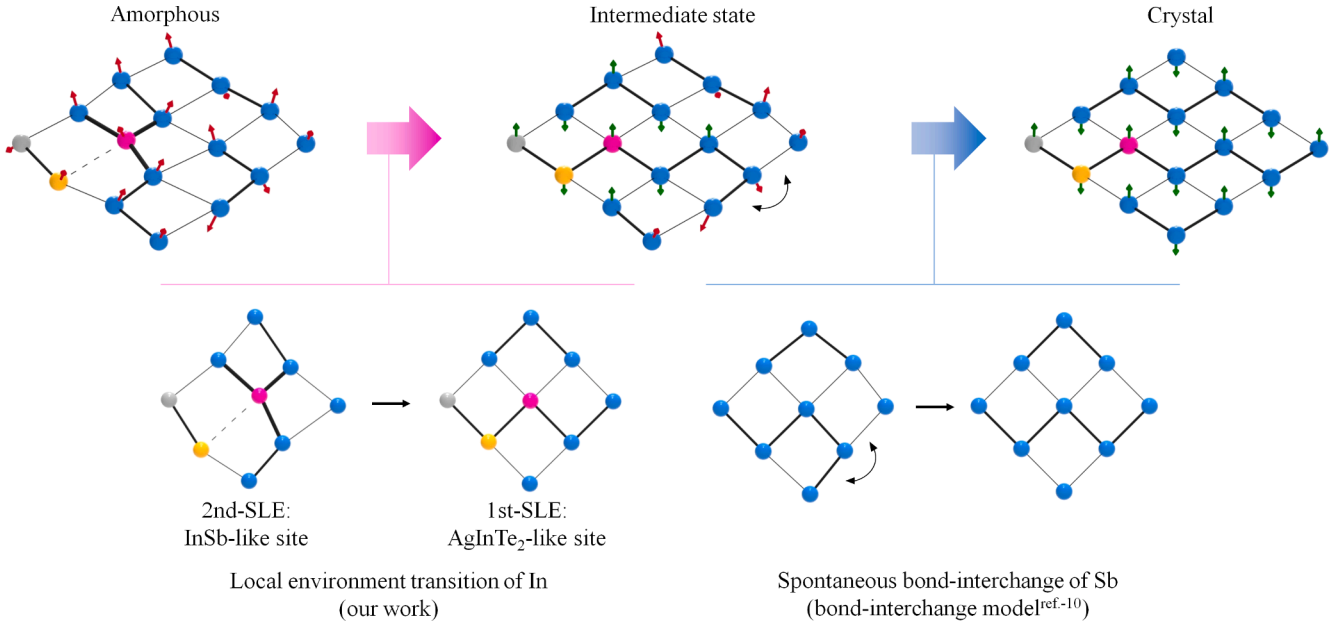

Fig. 7. Crystallization mechanism of Ag-In-Sb-Te. Three-dimensional atomic configurations of crystalline and amorphous AIST are simplified into a two-dimensional scheme. Ag, In, Sb, and Te atoms are colored silver, magenta, sky blue, and yellow, respectively. Vectors, pointing the direction of the sum of short bonds of each atom to visualize the degree of atomic alignment are introduced, where misaligned and aligned vectors are colored red and green, respectively. Crystallization process of Ag-In-Sb-Te is a two-step process, local environment transition of In and bond-interchange of Sb. Local environment transition of In from second stable local environment (2nd-SLE) of AIST to first stable local environment (1st-SLE), which are InSb-like to $AgInTe_2$-like site, respectively, occurs at the first step of crystallization. Subsequently, spontaneous bond-interchange of Sb occurs to align with adjacent atoms for crystallization. (For interpretation of the references to color in this figure legend, the reader is referred to the web version of this article.)

mechanism of AIST at atomic scale as a two-step process, as pictured in Fig. 7 [10]. Vectors are introduced to visualize the degree of atomic alignment by pointing the direction of the sum of short bonds of each atom, where misaligned (well aligned) ones with adjacent atoms are coloured red (green). At the amorphous phase, In in InSb-like site suppresses spontaneous bond-interchange of Sb and stabilizes misaligned vectors (atomic alignment). When enough Joule heats for crystallization are provided, it derives transition of local environment of In from InSb-like to $AgInTe_2$-like site. Subsequently, spontaneous bond-interchange between short and long bonds of Sb to align with adjacent atoms is followed until every vector becomes aligned, i.e., crystalline phase. (It is worth to re-note that crystallization temperature of pure Sb is below the room temperature.) As In directly obstructs (or allows) spontaneous bond-interchange of Sb by transition of local environment, we can compare the role of In to that of a *dam* built to prevent an *avalanche,* bond-interchange of Sb.

The transition of local environment of In from InSb-like site becomes difficult without the element Ag in AIST; i.e., the presence of Ag positively affects the structural flexibility to enable transition of local environment of In from the InSb-like site. In this context, we can compare the role of Ag to that of a *gate* in the *dam* wall. That is, the role of In in $AgInTe_2$-like (InSb-like) sites can be compared to that of a *dam* with open (closed) *gates* to allow (prevent) an *avalanche*. Without *gates* in the *dam* wall, *avalanche* process cannot be effectively operated due to blocking of *dam,* i.e., without Ag, bond-interchange of Sb is suppressed by residual In in InSb-like site. Te can be compared to a connection

centre of chemical bonds, comprising bonds with every element in AIST except with Te itself (Ag, In, and Sb). Specifically, Ag, In, and Sb play their respective roles, extending and shortening their own bonds with Te. These results led us to propose the "dam-gate" model to describe the roles of Ag, In, and Te in AIST.

The transition of chemical bonds at the core level and in the valence band during the crystallization of $AIST_{Eutectic}$ (denoted by the red circle in Fig. 1 a) was ascertained to be identical to that of AIST (denoted by the blue circle in Fig. 1 a) as shown in Figs. 2, 3, and 5. It indicates that the local environments and roles of Ag, In, and Te in $AIST_{Eutectic}$ are consistent with the dam-gate model of AIST. The dam-gate model accounts for the unexplained experimental results of thermal stability depending on the composition of Ag-In-Sb-Te. Crystallization temperature largely increases by increasing the composition of In and decreasing the composition of Ag when comparing $Ag_4In_{11.1}Sb_{56.8}Te_{28.1}$ (199 °C) with $Ag_{12.4}In_{3.8}Sb_{55}Te_{27.8}$ (170 °C) [56] (denoted by orange circles in Fig. 1 a [56–60]). As the number of *dam* (In) increases and that of *gate* (Ag) decreases, the activation energy to open the closed *gate* of *dam* (to change local environment from InSb-like to $AgInTe_2$-like site) increases which leads the increase of crystallization temperature. On the other hand, crystallization temperature also increases by decreasing the composition of Sb and increasing the composition of Te when comparing $AIST_{Eutectic}$ (170 °C–200 °C) [23,25–28] with AIST (~160 °C) [49,51,61]. As the number of driving element of *avalanche* (Sb) decreases and that of connection center (Te) increases, momentum for *avalanche* process (atomic alignments driven by bond-interchange of Sb) decreases and it leads to increase of crystallization temperature. The experimental results of thermal stability depending on composition in Ag-In-Sb-Te could hitherto not be explained based on the other existing models. Zhu *et al.* recently reported that Ag and In occupy Sb sites in phase-separated Sb_2Te_3 to bond with Te in $Ag_{5.13}In_{3.32}Sb_{65.60}Te_{25.93}$ (denoted by the red circle in Fig. 1 a) when annealed above the crystallization temperature [11]. It is consistent with our results, according to which, Ag, In, and Te consist of a $AgInTe_2$-like bonding topology in the crystalline state. Based on the additional MD simulations, they suggested that both Ag and In stabilize the amorphous phase, while In additionally promotes rate of crystallization. At the atomic scale, our experimental data and the dam-gate model can account for the MD simulation, i.e., the element In in InSb-like site stabilizes the amorphous phase, whereas In in $AgInTe_2$-like site suppresses the high diffusivity of Ag and promotes the rate of crystallization. Dam-gate model successfully accounts for the experimental results at the various compositions in Ag-In-Sb-Te, which suggests that applicability of the dam-gate model illustrating the role of each element at atomic scale can be extended from AIST to Ag-In-Sb-Te.

The dam-gate model and other reported models such as bond-interchange model and recent result on crystalline $Ag_{5.13}In_{3.32}Sb_{65.60}Te_{25.93}$, all of which clarify the roles of the constituent elements in the crystallization of Ag-In-Sb-Te, remind us of the umbrella flip model as a crystallization mechanism in the most popular PCM, Ge-Sb-Te. In Ge-Sb-Te, the element Ge is responsible for the local environment transition between tetrahedral (or defective octahedral) and octahedral sites. It corresponds to In in Ag-In-Sb-Te because local environment transition during the crystallization of AIST is induced by In. Moreover, Sb acts as a vacancy former in Ge-Sb-Te, in which the fabricated vacancies provide structural flexibility for Ge to change local environments, which enhances the cyclability and phase-change rate in Ge-Sb-Te [3,62]. This corresponds to the role of Ag in Ag-In-Sb-Te because Ag provides structural flexibility for In in Ag-In-Sb-Te. In addition, Te acts as a backbone in Ge-Sb-Te, which assists Ge, Sb, and vacancies to perform their respective roles during phase change by extending or shortening its own bonds with Te. This corresponds to the role of Te in AIST as a connection hub. It is remarkable that role of Te in both Ag-In-Sb-Te and Ge-Sb-Te is alike to connection hub, while Sb in Ag-In-Sb-Te (driving element for crystallization) is clearly differentiated with that in Ge-Sb-Te (vacancy former).

Finally, based on the precedent reports and our dam-gate model, the orbital configurations of each element during phase-change of Ag-In-Sb-Te can be obtained [10,11]. Ag conveys its $5\,s^1$ electron to Te and forms ionic bonding in both amorphous and crystalline Ag-In-Sb-Te. The orbital configurations of the element In in its local environments are clearly differentiated: i.e., those in $AgInTe_2$-like and InSb-like site can be represented by $5p^3$ and $5sp^3$, respectively, where deficient electrons are compensated from Te or Sb. Orbital configurations of Te are rather complex but mainly compose of $5p^3$ in both amorphous and crystalline Ag-In-Sb-Te, which are identical with those of Sb [10].

4. Conclusions

Element In dramatically changes its chemical bonding from Sb-bonds (In-Sb) to Te-bonds (In-Te) upon crystallization of Ag-In-Sb-Te, while the other elements negligibly change its chemical bonding. The local environment of In which mainly bonds with Te (Sb) in Ag-In-Sb-Te is characterized as $AgInTe_2$-like (InSb-like) site. The structural characteristics of the suggested local environments are experimentally verified with electrical/optical macroscopic techniques. In critically modulates the degree of atomic ordering and activation energy for crystallization despite of low composition of In (4%). The results suggest that crystallization mechanism is deployed by transition of local environment of element In from InSb-like to $AgInTe_2$-like site. The crystallization mechanism of Ag-In-Sb-Te at atomic scale reveals role of constituent element in Ag-In-Sb-Te: Ag provides structural flexibility for local environment transition of In, In disrupts crystallization, and Te assists the other elements to play their respective roles. The roles of Ag, In, and Te are compared to those of the *gate* of a *dam*, a *dam* preventing an *avalanche*, and the connection centre of chemical bonds, respectively. Eventually, we account for the unexplained experimental reports and compare role of element in Ag-In-Sb-Te with those in the most well-known PCM, Ge-Sb-Te.

Our study represents the first attempt to clarify crystallization mechanism based on the results of chemical bond evolution upon crystallization of PCMs, which is especially effective method in the cases that instrumental methods for local structural characteristics such as XAS are technically limited. Our results on role of Ag, In, and Te, which adequately controls spontaneous atomic alignments of Sb, successfully account for unique phase-change mechanism of Ag-In-Sb-Te at atomic scale, clearly differentiated with the other PCMs such as Ge-Sb-Te or Ti-Sb-Te. We expect our report to spark the development of rapid and energy efficient PCMs beyond Ag-In-Sb-Te, based on the control of spontaneous atomic alignments.

Author contribution

Dasol Kim: Conceptualization, Data curation, Writing. **Taek Sun Jung:** Data curation. **Hanjin Park:** Data curation. **Wonjun Yang:** Methodology. **Jeonghwa Han:** Methodology. **Soobin Hwang:** Methodology. **Kyung Ik Sim:** Software. **Young-Kyun Kwon:** Data curation. **Jae Hoon Kim:** Data curation. **Mann-Ho Cho:** Project administration.

Declaration of Competing Interest

The authors declare that they have no known competing financial interests or personal relationships that could have appeared to influence the work reported in this paper.

Acknowledgments

This work was supported by the Ministry of Trade, Industry & Energy (MOTIE) in Korea (Project No. 10080625) and the Korea Semiconductor Research Consortium (KSRC) through a project for developing source technologies for future semiconductor devices and the Nano Material Technology Development Program through the National Research

Foundation of Korea (NRF) funded by the Ministry of Science, ICT, and Future Planning (NRF-2016M3A7B4910398).

Appendix A. Supplementary material

Supplementary data to this article can be found online at https://doi.org/10.1016/j.apsusc.2020.148838.

References

[1] Q. Xia, J.J. Yang, Memristive crossbar arrays for brain-inspired computing, Nat. Mater. 18 (2019) 309–323, https://doi.org/10.1038/s41563-019-0291-x.
[2] Z. Wang, H. Wu, G.W. Burr, K.L. Wang, Q. Xia, J.J. Yang, Resistive switching materials, Nat. Rev. Mater. (n.d.). 10.1038/s41578-019-0159-3.
[3] A.V. Kolobov, P. Fons, A.I. Frenkel, A.L. Ankudinov, J. Tominaga, T. Uruga, Understanding the phase-change mechanism of rewritable optical media, Nat. Mater. 3 (2004) 703–708, https://doi.org/10.1038/nmat1215.
[4] B. Huang, J. Robertson, Bonding origin of optical contrast in phase-change memory materials, Phys. Rev. B - Condens. Matter Mater. Phys. 81 (2010) 1–4, https://doi.org/10.1103/PhysRevB.81.081204.
[5] F. Rao, Z. Song, Y. Cheng, X. Liu, M. Xia, W. Li, K. Ding, X. Feng, M. Zhu, S. Feng, Direct observation of titanium-centered octahedra in titanium–antimony–tellurium phase-change material, Nat. Commun. 6 (2015) 1–6, https://doi.org/10.1038/ncomms10040.
[6] M. Zhu, M. Xia, F. Rao, X. Li, L. Wu, X. Ji, S. Lv, Z. Song, S. Feng, H. Sun, S. Zhang, One order of magnitude faster phase change at reduced power in Ti-Sb-Te, Nat. Commun. 5 (2014) 1–6, https://doi.org/10.1038/ncomms5086.
[7] R.E. Simpson, P. Fons, A.V. Kolobov, T. Fukaya, M. Krbal, T. Yagi, J. Tominaga, Interfacial phase-change memory, Nat. Nanotechnol. 6 (2011) 501–505, https://doi.org/10.1038/nnano.2011.96.
[8] Y. Zhou, R. Mazzarello, Z. Song, S. Lv, I. Ronneberger, M. Xia, K. Ding, W. Zhang, F. Rao, S. Feng, E. Ma, Y. Zheng, Reducing the stochasticity of crystal nucleation to enable subnanosecond memory writing, Science (80-.). 358 (2017) 1423–1427. 10.1126/science.aao3212.
[9] K. Ding, J. Wang, Y. Zhou, H. Tian, L.L. Lu, R. Mazzarello, C. Jia, W. Zhang, F. Rao, E. Ma, Phase-change heterostructure enables ultralow noise and drift for memory operation, Science (80-.). 366 (2019) 210–215. 10.1126/science.aay0291.
[10] T. Matsunaga, J. Akola, S. Kohara, T. Honma, K. Kobayashi, E. Ikenaga, R.O. Jones, N. Yamada, M. Takata, R. Kojima, From local structure to nanosecond recrystallization dynamics in AgInSbTe phase-change materials, Nat. Mater. 10 (2011) 129–134, https://doi.org/10.1038/nmat2931.
[11] M. Zhu, W. Song, P.M. Konze, T. Li, B. Gault, X. Chen, J. Shen, S. Lv, Z. Song, M. Wuttig, R. Dronskowski, Direct atomic insight into the role of dopants in phase-change materials, Nat. Commun. 10 (2019) 1–10, https://doi.org/10.1038/s41467-019-11506-0.
[12] K. Dayal Shukla, N. Saxena, S. Durai, A. Manivannan, Redefining the speed limit of phase change memory revealed by time-resolved steep threshold- switching dynamics of AgInSbTe Devices, Sci. Rep. 6 (2016) 1–7, https://doi.org/10.1038/srep37868.
[13] W.K. Njoroge, M. Wuttig, Crystallization kinetics of sputter-deposited amorphous AgInSbTe films, J. Appl. Phys. 90 (2001) 3816–3821, https://doi.org/10.1063/1.1405141.
[14] H. Iwasaki, M. Harigaya, O. Nonoyama, Y. Kageyama, M. Takahashi, K. Yamada, H. Deguchi, Y. Ide, Completely Erasable Phase Change Optical Disc II- Application of Ag-In-Sb-Te Mixed-Phase System for Rewritable Compact Disc Compatible with CD-Velocity and Double CD-Velocity, Japanese J. Appl. Phys. Part 1-Regular Pap. Short Notes Rev. Pap. 32 (1993) 5241–5247. 10.1143/JJAP.32.5241.
[15] J. Li, F. Gan, Optical properties of Ag 8 In 14 Sb 55 Te 23 phase-change films, Thin Solid Films. 402 (2002) 232–236.
[16] F.X. Zhai, K. Yang, D. Wang, S. Liu, N. Liu, Y. Hao, Y. Ren, Bipolar resistive switching effect in laser-induced crystallization AgInSbTe films, Optik (Stuttg). 180 (2019) 271–275, https://doi.org/10.1016/j.ijleo.2018.11.100.
[17] P. Zalden, F. Quirin, M. Schumacher, J. Siegel, S. Wei, A. Koc, M. Nicoul, M. Trigo, P. Andreasson, H. Enquist, M.J. Shu, T. Pardini, M. Chollet, D. Zhu, H. Lemke, I. Ronneberger, J. Larsson, A.M. Lindenberg, H.E. Fischer, S. Hau-Riege, D.A. Reis, R. Mazzarello, M. Wuttig, K. Sokolowski-Tinten, Femtosecond X-ray diffraction reveals a liquid-liquid phase transition in phase-change materials, Science (80-.). 364 (2019) 1062–1067.
[18] J. Orava, D.W. Hewak, A.L. Greer, Fragile-to-Strong Crossover in Supercooled Liquid Ag-In-Sb-Te Studied by Ultrafast Calorimetry, Adv. Funct. Mater. 25 (2015) 4851–4858, https://doi.org/10.1002/adfm.201501607.
[19] J. Orava, H. Weber, I. Kaban, A.L. Greer, Viscosity of liquid Ag-In-Sb-Te: Evidence of a fragile-to-strong crossover, J. Chem. Phys. 144 (2016), https://doi.org/10.1063/1.4949526.
[20] M. Salinga, E. Carria, A. Kaldenbach, M. Bornhöfft, J. Benke, J. Mayer, M. Wuttig, Measurement of crystal growth velocity in a melt-quenched phase-change material, Nat. Commun. 4 (2013) 2371, https://doi.org/10.1038/ncomms3371.
[21] W. Zhang, I. Ronneberger, P. Zalden, M. Xu, M. Salinga, M. Wuttig, R. Mazzarello, How fragility makes phase-change data storage robust: Insights from ab initio simulations, Sci. Rep. 4 (2014) 2–7, https://doi.org/10.1038/srep06529.
[22] P. Zalden, A. Von Hoegen, P. Landreman, M. Wuttig, A.M. Lindenberg, How Supercooled Liquid Phase-Change Materials Crystallize: Snapshots after Femtosecond Optical Excitation, Chem. Mater. 27 (2015) 5641–5646, https://doi.org/10.1021/acs.chemmater.5b02011.
[23] S. Sahu, A. Manivannan, H. Shaik, G. Mohan Rao, Local structure of amorphous Ag5In5Sb60Te30 and In3SbTe2 phase change materials revealed by X-ray photoelectron and Raman spectroscopic studies, J. Appl. Phys. 122 (2017) 015305-1–5. 10.1063/1.4991491.
[24] W. Zhang, R. Mazzarello, M. Wuttig, E. Ma, Designing crystallization in phase-change materials for universal memory and neuro-inspired computing, Nat. Rev. Mater. 4 (2019) 150–168, https://doi.org/10.1038/s41578-018-0076-x.
[25] C.C. Chou, F.Y. Hung, T.S. Lui, Role of crystallized phases in sheet resistance of amorphous AgInSbTe chalcogenide film, Scr. Mater. 56 (2007) 1107–1110, https://doi.org/10.1016/j.scriptamat.2007.02.005.
[26] J.J. Zhang, H.J. Sun, Y. Li, Q. Wang, X.H. Xu, X.S. Miao, AgInSbTe memristor with gradual resistance tuning, Appl. Phys. Lett. 102 (2013) 183513-1–4. 10.1063/1.4804983.
[27] J. Singh, D.K. Aswal, S.K. Gupta, Annealing induced structural changes in sputtered AgInSbTe thin films and its implication on electrical properties, Mater. Res. Express. 2 (2015) 066403-1–8. 10.1088/2053-1591/2/6/066403.
[28] J. Tominaga, T. Kikukawa, M. Takahashi, R.T. Phillips, Structure of the optical phase change memory alloy, Ag-V-In-Sb-Te, determined by optical spectroscopy and electron diffraction, J. Appl. Phys. 82 (1997) 3214–3218, https://doi.org/10.1063/1.365627.
[29] H. Tashiro, M. Harigaya, Y. Kageyama, K. Ito, M. Shinotsuka, K. Tani, A. Watada, N. Yiwata, Y. Nakata, S. Emura, Structural analysis of Ag-In-Sb-Te phase-change material, Japanese J. Appl. Physics, Part 1 Regul. Pap. Short Notes Rev. Pap. 41 (2002) 3758–3759, https://doi.org/10.1143/JJAP.41.3758.
[30] W.H. Zachariasen, The atomic arrangement in glass, J. Am. Chem. Soc. 54 (1932) 3841–3851, https://doi.org/10.1021/ja01349a006.
[31] C.A. Schuh, T.C. Hufnagel, U. Ramamurty, Mechanical behavior of amorphous alloys, Acta Mater. 55 (2007) 4067–4109, https://doi.org/10.1016/j.actamat.2007.01.052.
[32] W.K. and L.J. Sham, Self-Consistent Equations Including Exchange and Correlation Effects*, Phys. Rev. 140 (1965) A1133–A1138. 10.1046/j.1365-4362.2002.01376.x.
[33] and J.M.S. Ordejon, Pablo; Emilio Artacho, Self-consistent order-N density-functional calculations for very large systems, Phys. Rev. B. 53 (1996) R10 441-R10 444. 10.1103/PhysRevB.53.R10441.
[34] Jos, M. Soler, A. Emilio, D.G. Julian, G. Alberto, J. Javier, O. Pablo, S. Daniel, P. Nchez, The SIESTA method for ab initio order-N materials simulation, J. Phys. Condens. Matter. (2002) 2745–2779. file://c/Users/seabra/Documents/Work/Literature/Articles/SIESTA_2002.pdf.
[35] N. Troullier, J.L. Martins, Efficient pseudopotentials for plane-wave calculations, Phys. Rev. B. 43 (1993) 1993–2006, https://doi.org/10.1103/PhysRevB.43.1993.
[36] D.M. Bylander, L. Kleinman, Efficacious Form for Model Pseudopotentials, Phys. Rev. Lett. 48 (1982) 1425–1428.
[37] J.P. Perdew, E.R. McMullen, A. Zunger, Density-functional theory of the correlation energy in atoms and ions: A simple analytic model and a challenge, Phys. Rev. A. 23 (1981) 2785–2789, https://doi.org/10.1103/PhysRevA.23.2785.
[38] B.J. Alder, D. Ceperley, Ground State of the Electron Gas by a Stochastic Method, Phys. Rev. Lett. 45 (1980) 566–569.
[39] S. Nosé, S. Nosi~, Molecular Physics: An International Journal at the Interface Between Chemistry and Physics A molecular dynamics method for simulations in the canonical ensemble A molecular dynamics method for simulations in the canonical ensemblet, An Int. J. Interface Between Chem. Phys. Mol. Phys. 52 (1984) 255–268. 10.1080/00268978400101201.
[40] W.G. Hoover, Canonical dynamics: Equilibrium phase-space distributions, Phys. Rev. A. 31 (1965) 1695, https://doi.org/10.1007/BF00419952.
[41] M.P. Allen, D.J. Tildesley, Computer simulation of Liquids, Oxford University Press, 1989.
[42] D.C. Rapaport, The art of molecular Dynamics simulation, 2nd edn, Cambridge University Press, 2004.
[43] A. Klein, H. Dieker, B. Sp??th, P. Fons, A. Kolobov, C. Steimer, M. Wuttig, Changes in electronic structure and chemical bonding upon crystallization of the phase change material GeSb2Te4, Phys. Rev. Lett. 100 (2008) 1–4. 10.1103/PhysRevLett.100.016402.
[44] O.A. Balitskii, W. Jaegermann, XPS study of InTe and GaTe single crystals oxidation, Mater. Chem. Phys. 97 (2006) 98–101, https://doi.org/10.1016/j.matchemphys.2005.07.055.
[45] G.E.M. C.D. Wagner, W.M. Riggs, L.E. Davis, J.F. Moulder, Handbook of X Ray Photoelectron Spectroscopy_ A Reference Book of Standard Spectra data for use in X-ray Photoelectron spectroscopy, 1995.
[46] A. Chaturvedi, G.S. Varma, S. Asokan, U. Ramamurty, Physical and mechanical properties of intermediate phase chalcogenide glasses with centroid compositions in the Ge-Te-In-Ag system, J. Non. Cryst. Solids. 543 (2020), 120112, https://doi.org/10.1016/j.jnoncrysol.2020.120112.
[47] C.H. Kuo, J.M. Wu, S.J. Lin, Room temperature-synthesized vertically aligned InSb nanowires: Electrical transport and field emission characteristics, Nanoscale Res. Lett. 8 (2013) 1–8, https://doi.org/10.1186/1556-276X-8-69.
[48] E.K. Kim, D. Park, N.K. Shrestha, J. Chang, C.W. Yi, S.H. Han, A facile room temperature chemical transformation approach for binder-free thin film formation of Ag 2 Te and lithiation/delithiation chemistry of the film, Dalt. Trans. 45 (2016) 17312–17318, https://doi.org/10.1039/c6dt03038f.
[49] T. Matsunaga, R. Kojima, N. Yamada, Y. Kubota, K. Kifune, Structural transformation of Sb-based high-speed phase-change material, Acta Crystallogr. Sect. B Struct. Sci. 68 (2012) 559–570, https://doi.org/10.1107/S0108768112039961.

[50] K. Kifune, T. Fujita, T. Tachizawa, Y. Kubota, N. Yamada, T. Matsunaga, Crystal structures of X-phase in the Sb-Te binary alloy system, Cryst. Res. Technol. 48 (2013) 1011–1021, https://doi.org/10.1002/crat.201300252.
[51] T. Matsunaga, Y. Umetani, N. Yamada, Structural study of a Ag3.4In3.7Sb76.4Te16.5 quadruple compound utilized for phase-change optical disks, Phys. Rev. B - Condens. Matter Mater. Phys. 64 (2001) 184116-1–7. 10.1103/PhysRevB.64.184116.
[52] K. Shportko, S. Kremers, M. Woda, D. Lencer, J. Robertson, M. Wuttig, Resonant bonding in crystalline phase-change materials, Nat. Mater. 7 (2008) 653–658, https://doi.org/10.1038/nmat2226.
[53] M. Wuttig, V.L. Deringer, X. Gonze, C. Bichara, J.-Y. Raty, Incipient Metals: Functional Materials with a Unique Bonding Mechanism, Adv. Mater. 30 (2018) 1803777(1–6). 10.1002/adma.201803777.
[54] M. Salinga, B. Kersting, I. Ronneberger, V.P. Jonnalagadda, X.T. Vu, M. Le Gallo, I. Giannopoulos, O. Cojocaru-Mirédin, R. Mazzarello, A. Sebastian, Monatomic phase change memory, Nat. Mater. (2018), https://doi.org/10.1038/s41563-018-0110-9.
[55] R.L. Blaine, H.E. Kissinger, Homer Kissinger and the Kissinger equation, Thermochim. Acta. 540 (2012) 1–6, https://doi.org/10.1016/j.tca.2012.04.008.
[56] Y.C. Her, H. Chen, Y.S. Hsu, Effects of Ag and In addition on the optical properties and crystallization kinetics of eutectic Sb70Te30 phase-change recording film, J. Appl. Phys. 93 (2003) 10097–10103, https://doi.org/10.1063/1.1575493.
[57] C. Rangasami, Phase preference in some Ag-In-Sb-Te alloys, 1832 (2017) 140008-1–3. 10.1063/1.4980790.
[58] Y.C. Hang, L.C. Hou, Erasing Mechanisms of Ag – In – Sb – Te Compact Disk (CD), -Rewritable 39 (2000) 294–296.
[59] and masahiro okuda Tatsuhiko Matsushita, akio suzuki, tomoki nishiguchi, keiji shibata, Related content Phase-Change Optical Recording Films with AgInTe 2 – Sb – Te System, Jpn. J. Appl. Phys. Part 1 No. 2A. 34 (1995) 519–520.
[60] M. Krbal, A.V. Kolobov, P. Fons, J. Haines, A. Pradel, M. Ribes, A.A. Piarristeguy, C. Levelut, R. Le Parc, V. Agafonov, M. Hanfland, J. Tominaga, Pressure-induced structural transitions in phase-change materials based on Ge-free Sb-Te alloys, Phys. Rev. B - Condens. Matter Mater. Phys. 83 (2011) 1–5, https://doi.org/10.1103/PhysRevB.83.024105.
[61] S. Kimura, K. Kato, S. Kohara, Y. Moritomo, T. Matsunaga, Time-Resolved Investigation of Nanosecond Crystal Growth in Rapid-Phase-Change Materials: Correlation with the Recording Speed of Digital Versatile Disc, Media 1 (2008) 4–6, https://doi.org/10.1143/APEX.1.045001.
[62] M. Wuttig, D. Lüsebrink, D. Wamwangi, W. Wełnic, M. Gilleßen, R. Dronskowski, The role of vacancies and local distortions in the design of new phase-change materials, Nat. Mater. 6 (2007) 122–128, https://doi.org/10.1038/nmat1807.